

# A compact polarization-integrated long wavelength infrared focal plane array based on InAs/GaSb superlattice

Jian ZHOU<sup>1</sup>, Yi ZHOU<sup>1,2\*</sup>, Ying SHI<sup>1</sup>, Fangfang WANG<sup>1</sup>, Zhicheng XU<sup>1</sup>,  
Zhizhong BAI<sup>1</sup>, Min HUANG<sup>1</sup>, Lulu ZHENG<sup>1</sup>, Zhaoming LIANG<sup>1</sup>, Yihong ZHU<sup>1</sup>,  
Qingqing XU<sup>1</sup>, Yiming SHEN<sup>1</sup>, Xiangxiao YING<sup>1</sup> & Jianxin CHEN<sup>1,2\*</sup>

<sup>1</sup>Key Laboratory of Infrared Imaging Materials and Devices, Shanghai Institute of Technical Physics,  
Chinese Academy of Sciences, Shanghai 200083, China;

<sup>2</sup>Hangzhou Institute for Advanced Study, University of Chinese Academy of Sciences, Hangzhou 310024, China

Received 27 January 2021/Revised 18 March 2021/Accepted 22 April 2021/Published online 6 January 2022

**Abstract** Real-time polarization imaging plays a vital role in target detection, recognition, and tracking in complex scenes. However, large optical crosstalk and the integration technology are difficult problems in the development of polarization-integrated infrared detectors. We demonstrate a monolithic long wavelength infrared (LWIR) InAs/GaSb superlattice focal plane array (FPA) integrated with the polarizer. To obtain high performance and real-time polarization imaging device, the parameters of the grating were optimized and the optical crosstalk between adjacent polarization bands was studied. We analysis the light diffraction depending on the distance between the polarizer and photosensitive elements, and the coupling between oblique incident light and device. The fabrication process of the antireflective polarizer, the integration technology of polarizer and the FPA composed of 512×4×3 pixels were explored. Finally, a polarization integrated focal plane array (PI-FPA) was fabricated to detect polarized light with different oscillating directions. The large response extinction ratio of corresponding polarization bands was measured as 50:1, 49:1, and 44:1 of 0°, 60°, and 120°, respectively.

**Keywords** LWIR, polarization integration, infrared detector, optical crosstalk, extinction ration

**Citation** Zhou J, Zhou Y, Shi Y, et al. A compact polarization-integrated long wavelength infrared focal plane array based on InAs/GaSb superlattice. *Sci China Inf Sci*, 2022, 65(2): 122407, <https://doi.org/10.1007/s11432-021-3252-2>

## 1 Introduction

As a fundamental characteristic of light, polarization describes the path of light's electric field vector oscillating in space-time, and one of its applications is of great interest in imaging technology [1–4]. Compared with the traditional imaging of intensity sensitivity, polarization imaging can capture more light information effectively, distinguish the intrinsic property polarization of artificial target and background, and improve the capability of target detection and recognition. The state-of-the-art micro-nano fabrication and integrated technology provide a promising platform for the compact monolithically polarization imaging of full-Stokes vector in real time [5–8], which overcomes the shortcomings of bulky optical systems, reliant on moving parts, and limited in time resolution. The long wavelength infrared (LWIR) detectors have advantages in some facilities camouflage and false target recognition. The InAs/GaSb of type II superlattice (T2SL) is an excellent candidate material in long wavelength infrared detection thanks to its unique material properties, including tunable band gaps, low dark current, high quality of uniformity, and low cost [9–12]. Subwavelength gratings integrated on a focal plane arrays (FPAs) for near-infrared (NIR) and mid-infrared (MIR) polarization imaging have been reported in [12–14]. The LWIR polarization integration focal plane array (PI-FPA) plays an important role in camouflaged target

\* Corresponding author (email: zhouyi@mail.sitp.ac.cn, jianxinchen@mail.sitp.ac.cn)

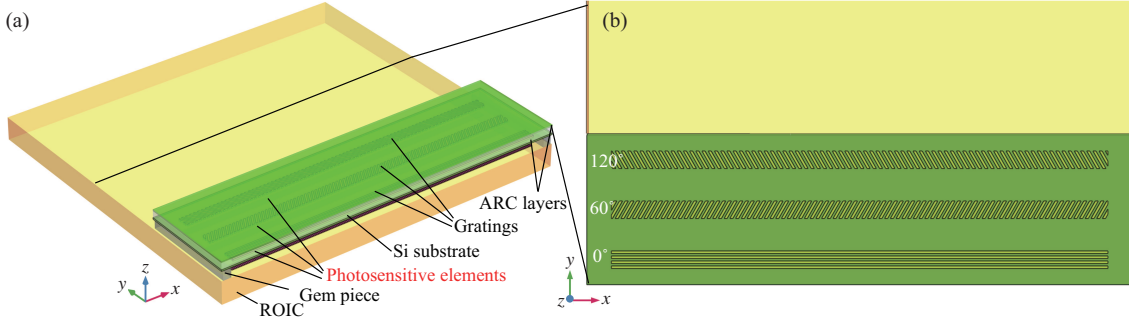


**Figure 1** (Color online) (a) Schematic diagram and (b)  $x$ - $y$  cross-sectional view of the designed long wavelength T2SL PI-FPA.

identifying at room temperatures using polarization information [15–20]. However, compared with the MIR detector, the detectivity of the LWIR detector is relatively weak due to the high dark current, and the integration of polarization gratings will lose a lot of optical signals, which will further reduce the signal-to-noise ratio of the device [21]. Furthermore, large optical crosstalk leads to a low extinction ratio, and the integration technology of polarization grating and detector are difficult problems in the development of polarization-integrated infrared detector [22, 23]. Up until now, those two hard problems have not been solved but the research on LWIR PI-FPA is very rare. Therefore, it is of great significance to develop a high extinction ratio and high transmission on-chip polarization detector. In this study, the FPA based on InAs/GaSb integrated with the polarizer of three polarizations bands was designed and fabricated. We focused on the study of optical crosstalk between adjacent polarization bands, explored the fabrication process of antireflective polarizers and the integration technology of PI-FPA with high extinction ratios over 40:1, which provides a theoretical basis and technical support for the new generation of PI-FPA application in long wavelength infrared imaging.

## 2 Design method and proposed structure

For polarization imaging, the Stokes-vector components, the degree of linear polarization (DOLP) and angle of polarization (AOP) need to be calculated as [5, 6, 24–26]

$$s = \begin{bmatrix} s_0 \\ s_1 \\ s_2 \end{bmatrix} = \frac{2}{3} \begin{bmatrix} I_0 + I_{60} + I_{120} \\ I_0 - I_{60} - I_{120} \\ \sqrt{3} \cdot (I_{120} - I_{60}) \end{bmatrix}, \quad (1)$$

$$\text{DOLP} = \frac{\sqrt{s_1^2 + s_2^2}}{s_0}, \quad (2)$$

$$\text{AOP} = \frac{1}{2} \arctan \frac{s_2}{s_1}, \quad (3)$$

where the symbols  $s_0$ ,  $s_1$ , and  $s_2$  refer to the three Stokes-vector components. To get polarization characteristics of the imaged object in real-time by a push-broom scanning pattern, a long wavelength PI-FPA was designed based on Type-II superlattice infrared detectors and a  $512 \times 4 \times 3$  read-out integrated circuit. The PI-FPA was designed to have 3 polarization bands ( $0^\circ$ ,  $60^\circ$ , and  $120^\circ$ ), as shown in Figure 1(a), and every band has  $512 \times 4$  pixels. Figure 1(b) shows the  $x$ - $y$  cross-sectional view of the designed PI-FPA, respectively. Three directions ( $0^\circ$ ,  $60^\circ$ , and  $120^\circ$ ) of polarization Al gratings were fabricated on the silicon substrate, and antireflection coating was deposited on two sides. Each band (4 pixels) of photosensitive element is completely covered by the  $0^\circ$ ,  $60^\circ$ , and  $120^\circ$  direction polarizer (8 pixels/band), respectively. The PI-FPA model in the  $x$ -direction can be assumed infinitely long, allowing the use of 2-D simulation. The polarization extinction ratio (ER) is the contrast between the transmission or absorption of transverse magnetic (TM) incidence light and that of transverse electric (TE) incidence light for polarizer or PI-FPA, respectively.

The schematic diagram of the subwavelength metal grating investigated is illustrated in Figure 2(a). The period, width, and height of the Al grating is  $p$ ,  $w$ , and  $h$ , respectively. To reduce the light loss from

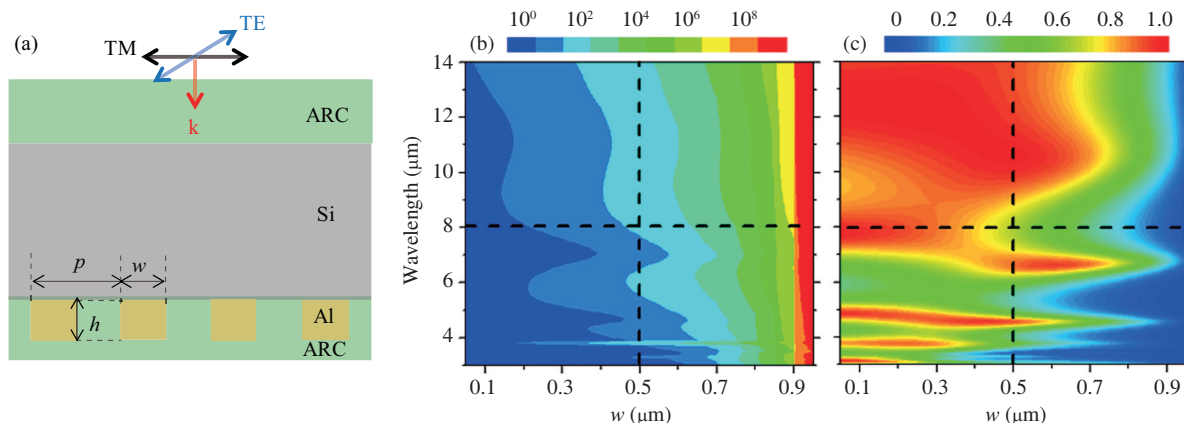


**Figure 2** (Color online) (a) Schematic diagram of the subwavelength metal grating; (b) ER and (c) TM light transmission spectra as functions of metal linewidth.

the surface reflection of the polarizer, a suitable antireflection coating (ARC) is required to enhance the transmission, which is designed to be composed of ZnS and Ge layers. In the numerical simulation, the finite element method (FEM) was adopted to calculate the polarization ER which is the contrast between transmission of the TM wave and TE wave (see Appendix A for details). It is well known that the ER increases with the decrease of the grating period or the increase of the grating thickness [27, 28]. The optimized parameters of the grating can be seen in Appendix B. Considering that the minimum period resolution of grating fabricated by step lithography, and etching resistance of photoresist, the grating was designed as  $1\ \mu\text{m}$  in period and  $0.25\ \mu\text{m}$  in height. In practical applications, it is more important to balance the high ER and high TM light transmittance, which depends on the linewidth of the grating. Figures 2(b) and (c) show the ER and TM light transmittance spectra as functions of grating widths, respectively. It can be found that the ER increases with the increase of the metal linewidth, while the transmission of TM light decreases with the increase of the grating linewidth. The linewidth of the grating was set to be  $0.5\ \mu\text{m}$  to ensure the ER is greater than 100:1 and the average transmittance of TM light is greater than 90% in the wavelength range 8–14  $\mu\text{m}$ .

To further study the interaction between the polarizer and the focal plane array, the polarizer and FPA were designed as a whole, where  $d$  is the distance between the polarizer and photosensitive elements of FPA, as shown in Figure 3(a). The line/space/thickness of the grating is 500/500/250 nm, respectively. The polarizer is divided into three regions, where the gratings region and the “window” region include 8 lines, corresponding to the lines 12 to 19 and lines 42 to 49, which can reflect and transmit most of TE polarization light, respectively. When the polarizer is bonded to the chip, the photosensitive elements of lines 14 to 17 and lines 44 to 47 are covered by the gratings region and the “window” region, respectively. Another region is fully covered with Al film. Figure 3(b) shows the ER of absorption of the photosensitive element (line 16) with the different distances under normal illumination ( $\theta = 0^\circ$ ) at the wavelengths of 8, 9, 10, 11, and 12  $\mu\text{m}$ , respectively. The ER decreases with the increase of the distance between the polarizer and the chip. The results showed that the longer the wavelength is, the faster the extinction ratio decreases with the increase of distance, which is due to the stronger diffraction as it passes through the window region, leading to greater optical crosstalk. According to our simulation, the distance needs to be limited to 300  $\mu\text{m}$  to ensure the ER exceeds 100:1 in the wavelength range 8–12  $\mu\text{m}$ , which is also the goal of our integrated process.

If the ER of PI-FPA is very high only for the normal incident parallel light, but the ER for the incident light at a certain angle decreases sharply, which is no good effect of practical imaging. Considering the optical crosstalk caused by oblique incident light to the adjacent polarization bands, the extinction ratio of line 16 corresponding to different incident angles was calculated when the distance was 200  $\mu\text{m}$ , as shown in Figure 3(c). With the increase of incident angle, the ER of all wavelengths increases slightly and then decreases sharply. It is interesting that the ER reaches the largest when the incidence angle is  $15^\circ$ . To explore why the ER increases at a small angle ( $\leq 15^\circ$ ), Figure 3(d) gives the absorption of TM and TE as functions of angles of incident light at the wavelength of 10  $\mu\text{m}$ . It is found that both absorption of the TM and TE light increase with the increase of incident angle until  $15^\circ$ , which may be due to light being easier to couple to the photosensitive elements. Compared with the normal incidence of  $0^\circ$ , the optical

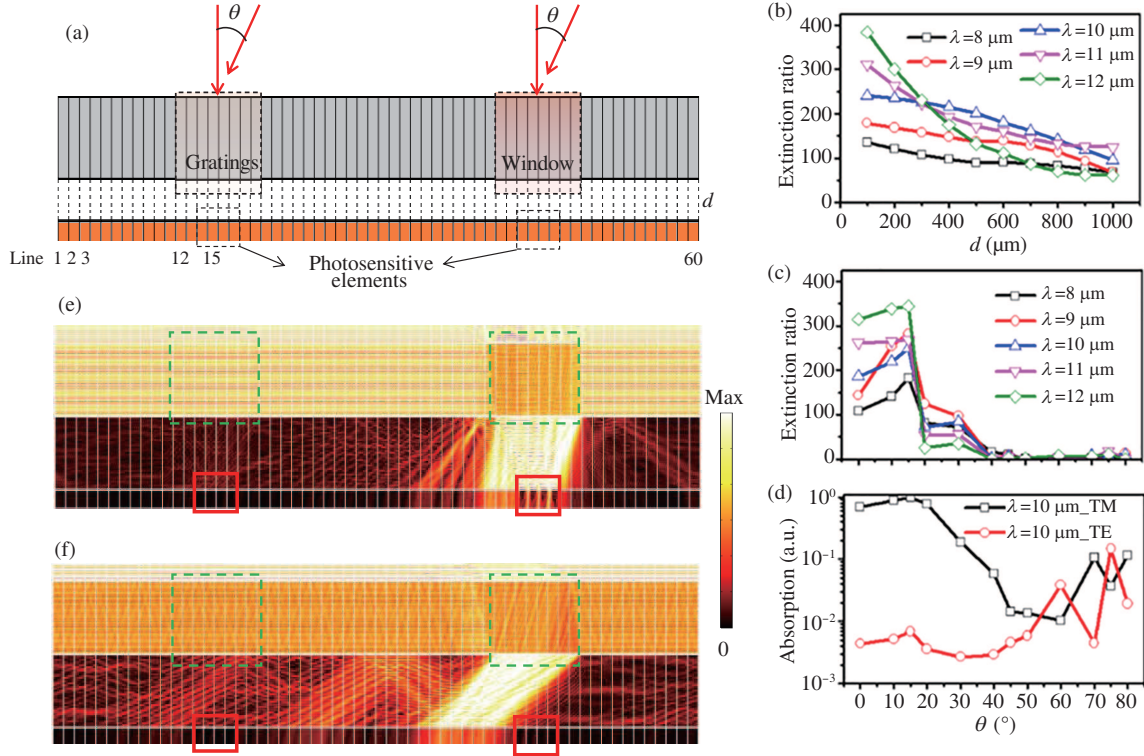


**Figure 3** (Color online) (a) The  $y$ - $z$  cross-sectional view of the PI-FPA; (b) the polarization extinction ratio of the absorption of the photosensitive element (line 16) as functions of distances between polarizers and photosensitizer under perpendicular illumination ( $\theta = 0^\circ$ ); (c) the extinction ratio of the absorption of the photosensitive element (line 16) at different angles of incidence; (d) the absorption of TM and TE as functions of angles of incident light. The optical field distribution of PI-FPA ( $d = 200 \mu\text{m}$ ) under TE polarization light incidence of (e)  $15^\circ$  and (f)  $45^\circ$  at the wavelength of  $10 \mu\text{m}$ , respectively.

field distribution within the photosensitive elements under TE polarization light incidence of  $15^\circ$  at the wavelength of  $10 \mu\text{m}$  is larger, as shown in Figure 3(e), which leads to an increase in TE light absorption. However, the absorption TM light increases faster than that of TE light, resulting in an increase in the ratio between them. With the angle of incidence continues to increase ( $>15^\circ$ ), both the TM and TE light absorption show a trend of decreasing and then increasing due to the propagation of waveguide in the cavity formed by the polarizer and FPA is more complex, which was illustrated by the optical field distribution of PI-FPA under TE polarization light incidence of  $45^\circ$  at the wavelength of  $10 \mu\text{m}$ , as shown in Figure 3(f), and the dynamic light propagation was displayed in Appendix Visualization on line. Considering the different requirements of F-number ( $F\#$ ) defined as the ratio of focal length to pupil diameter in the actual system application, it is inevitable that the radiation light of the target with a certain angle can be captured by the PI-FPA. The ER of PI-FPA ( $d = 200 \mu\text{m}$ ) is above 100:1 at the wavelength of  $10 \mu\text{m}$  when the incident angle is less than  $15^\circ$ .

### 3 Experiments, results, and discussions

The InAs/GaSb superlattice materials involved in this work were grown on n-type GaSb substrates by solid-source MBE. To reduce the absorption of light by n-GaSb substrate, a  $1.2 \mu\text{m}$  InAsSb layer was deposited on the substrate as a buffer for substrate corrosion. A PBIBN structure was designed to restrain the dark current density for long wavelength detectors. The absorption region consists of 300 periods superlattice and each period composed of 14 ML InAs/7 ML GaSb corresponding to a 50% cutoff wavelength over  $11 \mu\text{m}$  at 80 K. After growth, the wafer was processed into mesa-type focal plane arrays with the mesa size of  $27 \mu\text{m} \times 27 \mu\text{m}$  and isolation ditch width of  $3 \mu\text{m}$ . The mesas were passivated using  $\text{Si}_3\text{N}_4$  film. Ti/Pt/Au and Indium bumps were deposited on both the read-out integrated circuit and the arrays for flip-chip bonding. After flip-chip bonding, the GaSb substrate was completely removed.

In the fabrication process of polarizers, the  $500 \text{ nm}/500 \text{ nm}/250 \text{ nm}$  line/space/ thickness Al gratings were fabricated on Si by electron beam evaporation (EBE), step lithography (SL), and ion beam etching

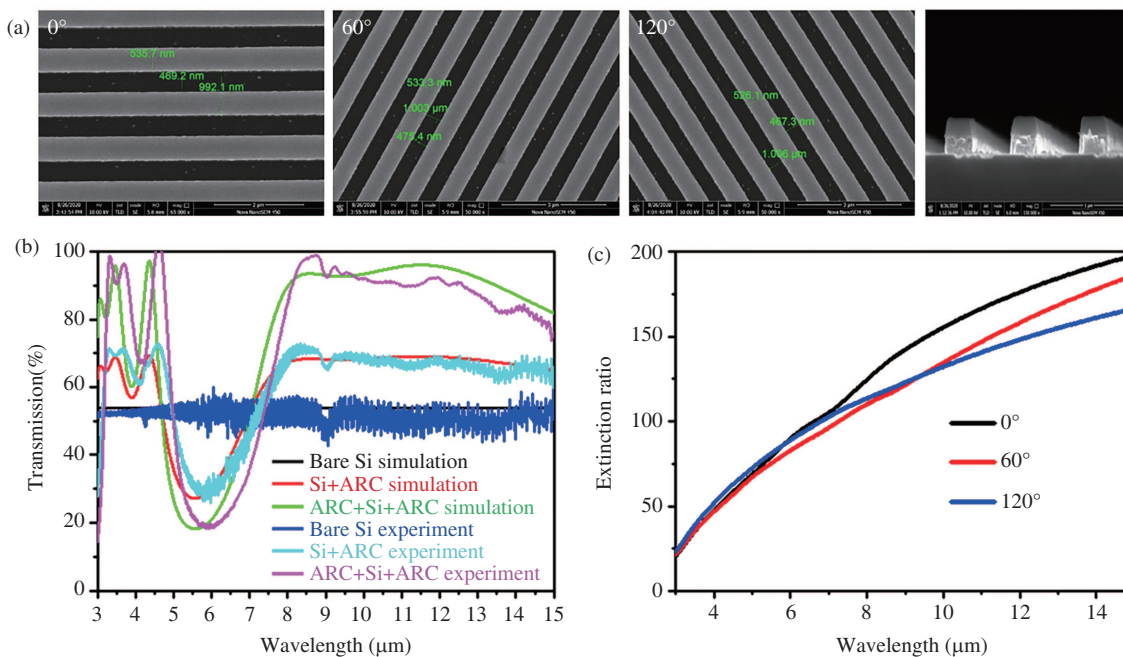


**Figure 4** (Color online) (a) Top-down SEM view of the fabricated Al gratings on Si with  $0^\circ$ ,  $60^\circ$ ,  $120^\circ$  polarization angles and cross section of grating; (b) the simulation and experimental transmission spectrum of Al gratings on Si without, with single side, with double sides ARC, respectively; (c) the experimental transmission extinction ratio spectra of Al gratings on Si with  $0^\circ$ ,  $60^\circ$ ,  $120^\circ$  polarization angles.

(IBE). Double sides ARC was demonstrated to further increase the transmittance. The polarizer is composed of 3 bands corresponding to  $0^\circ$ ,  $60^\circ$ ,  $120^\circ$ , respectively. One band grating area is  $15420 \mu\text{m} \times 240 \mu\text{m}$ , which can cover the photosensitive pixels region of the FPA. Figure 4(a) presents a micrograph by scanning electron microscopy (SEM) for the fabricated Al grating with  $0^\circ$ ,  $60^\circ$ ,  $120^\circ$  polarization angles, respectively. The line/spaces of Al gratings shown in Figure 4(a) are agreed with those of designed ones. Figure 4(b) gives the simulation and experimental transmittance spectrum of Al gratings on Si without, with one single side, with double sides ARC, respectively. Our simulation transmittance of bare Si substrate is about 54%, which is agreed with that of the above analysis data. The transmittance increases from about 54% to 68% and to 92% at the wavelength ( $10 \mu\text{m}$ ) after the Si substrate of one side and two sides were coated with ARC. It is noted that the experiment transmittance is slightly lower than the simulation value due to the thickness and roughness of each layer of thin-film being different from the ideal design value. Transmittance extinction ratios of Al gratings with  $0^\circ$ ,  $60^\circ$ ,  $120^\circ$  polarization angles were measured using a standard polarizer whose extinction ratio is about 1000:1. The results increase with the wavelength, shown in Figure 4(c) which is larger than 100 when the wavelength is greater than  $8 \mu\text{m}$ . The polarizer and FPA were bonded together utilizing the state-of-the-art of integrated technology, as shown in Figures 1(a) and 5(a). The polarizer was put on the gem piece coated with glue by the pixel alignment mark, and measured the distance from the back of the polarizer to the pixel to avoid damaging the photosensitive pixel and the readout circuit. The distance of  $z$ -direction between the grating surface and FPA was measured about at  $100 \mu\text{m}$ . The test system for measuring the polarization performance of PI-FPA includes a standard linear polarizer and traditional FPA testing system, and the polarizer was set between the black body and the dewar window. The polarized incident light with different polarization directions by rotating polarizer. The FPA has a 50% cutoff wavelength of  $11.7 \mu\text{m}$ . We focus on the key performance of PI-FPA, as shown in Table 1, including maximum responsivity (R) and root mean square (RMS) noise in comparison with those of the FPA without the polarizer.

With gradually rotating the angle of the polarizer from  $-5^\circ$  to  $190^\circ$ , the responsivity of PI-FPA reaches the maximum when the path of incident light's electric field vector oscillating is parallel to the polarization direction of the polarizer. The responsivity of PI-FPA was about half of the FPA without the polarizer, which indicates that the antireflection layer is very effective and only allows most TM polarized light to pass through the polarizer and to be absorbed by PI-FPA. Besides, the RMS Noise of FPA is stable after the polarizer is integrated, which indicates the integrating process did not deteriorate the dark current

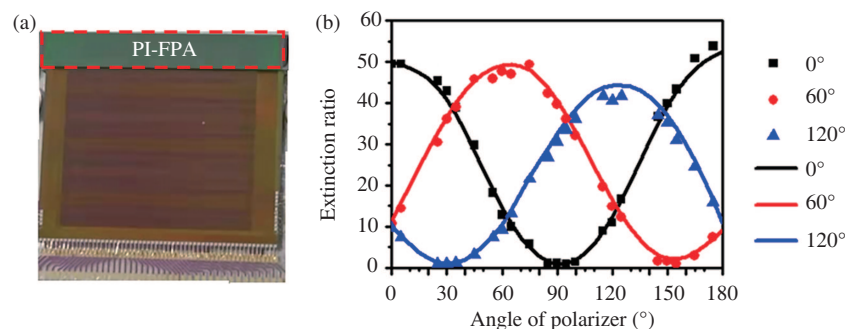


**Figure 5** (Color online) (a) The photograph of the fabricated PI-FPA; (b) the extinction ratio of PI-FPA of three bands ( $0^\circ$ ,  $60^\circ$ ,  $120^\circ$ ) as a function as the rotation angle of the polarizer in real time in test system. The scatter dot and solid line is the experimental and fitting data, respectively.

**Table 1** The key performance parameters of PI-FPA at 80 K without polarizer or with polarization band of  $0^\circ$ ,  $60^\circ$ , and  $120^\circ$ , respectively

|   | Without polarizer               | $0^\circ$ polarizer   | $60^\circ$ polarizer  | $120^\circ$ polarizer |
|---|---------------------------------|-----------------------|-----------------------|-----------------------|
| R (V/W)   | $5.64/5.84/5.77 \times 10^7$    | $3.02 \times 10^7$    | $3.26 \times 10^7$    | $3.23 \times 10^7$    |
| Peak detectivity ( $\text{Cm} \cdot \text{Hz}^{1/2} / \text{W}$ ) | $4.35/4.56/4.51 \times 10^{10}$ | $2.14 \times 10^{10}$ | $2.34 \times 10^{10}$ | $2.46 \times 10^{10}$ |
| Bad pixels rate (%)   | 6.25/1.17/1.56                  | 7.03                  | 1.17                  | 2.34                  |
| RMS noise (mV)  | 0.61/0.62/0.62                  | 0.6                   | 0.63                  | 0.61                  |

of the FPA.

To get the polarization performance of PI-FPA, Figure 5(b) gives the responsivity of PI-FPA of three bands ( $0^\circ$ ,  $60^\circ$ ,  $120^\circ$ ) as a function as the rotation angle of the polarizer, The ER of the band of  $0^\circ$ ,  $60^\circ$ , and  $120^\circ$  is obtained by data fitting is 50:1, 49:1, and 44:1, respectively. It indicates that the PI-FPA has significant characteristics of polarization detection. However, the extinction ratio of the experimental PI-FPA is lower than that of the design and the simulation one, which is the extinction ratio of the polarizer grating obtained in the experiment is lower than the design value, the distance between the polarizer and the detector is not close enough. Therefore, the fabrication technology of grating, the integration technology of polarizer and focal plane and the test system need to be further optimized and improved, only in this way can the performance of the PI-FPA be further enhanced. On the other hand, higher ER PI-FPA with mosaic super pixel structure will be studied in our later work, and part of the preliminary work is in Appendix C.

## 4 Conclusion

In summary, a compact InAs/GaSb FPA integrated with the polarizer composed of three polarization bands was designed and implemented. We analyzed the optical crosstalk between adjacent polarization bands, and explored the fabrication process of the antireflective polarizer and the integration technology of polarizer and FPA. Finally, a PI-FPA was fabricated to detect polarized light with different oscillating directions in real time. The extinction ratio of the corresponding polarization bands of  $0^\circ$ ,  $60^\circ$ , and  $120^\circ$  is 50:1, 49:1, and 44:1, respectively. The results of this work provide a way for the structural design, the fabrication process, and the integration technology of LWIR InAs/GaSb PI-FPA, as well as further expansion of polarization integrated detector of large array super pixel application scope in the long wavelength infrared polarization imaging, which will be studied in our later work.

**Acknowledgements** This work was supported by National Natural Science Foundation of China (NSFC) (Grant Nos. 61904183, 61974152, 61534006), National Key Research and Development Program of China (Grant No. 2016YFB0402403), Innovation Engineering Frontier Program of SITP, CAS (Grant No. 233), and Youth Innovation Promotion Association, CAS (Grant No. 2016219).

**Supporting information** Appendixes A–C. The supporting information is available online at [info.scichina.com](http://info.scichina.com) and [link.springer.com](http://link.springer.com). The supporting materials are published as submitted, without typesetting or editing. The responsibility for scientific accuracy and content remains entirely with the authors.

## References

- 1 Demos S G, Alfano R R. Optical polarization imaging. *Appl Opt*, 1997, 36: 150–155

- 2 Louie D C, Phillips J, Tchvialeva L, et al. Degree of optical polarization as a tool for detecting melanoma: proof of principle. *J Biomed Opt*, 2018, 23: 125004
- 3 Tong L, Huang X Y, Wang P, et al. Stable mid-infrared polarization imaging based on quasi-2D tellurium at room temperature. *Nat Commun*, 2020, 11: 2308
- 4 Ippolito S. Microscopy: polarized high-resolution imaging. *Nat Photon*, 2008, 2: 273–274
- 5 Rubin N A, D’Aversa G, Chevalier P, et al. Matrix Fourier optics enables a compact full-Stokes polarization camera. *Science*, 2019, 365: 1839
- 6 Ahmed A, Zhao X, Gruev V, et al. Residual interpolation for division of focal plane polarization image sensors. *Opt Express*, 2017, 25: 10651
- 7 Shi Z, Zhu A Y, Li Z, et al. Continuous angle-tunable birefringence with freeform metasurfaces for arbitrary polarization conversion. *Sci Adv*, 2020, 6: 3367
- 8 Osborne I S. A metasurface polarization camera. *Science*, 2019, 365: 40–42
- 9 Plis E A. InAs/GaSb type-II superlattice detectors. *Adv Electron*, 2014, 2014: 1–12
- 10 Rogalski A, Martyniuk P, Kopytko M. InAs/GaSb type-II superlattice infrared detectors: future prospect. *Appl Phys Rev*, 2017, 4: 031304
- 11 Delli E, Letka V, Hodgson P D, et al. Mid-infrared InAs/InAsSb superlattice nBn photodetector monolithically integrated onto silicon. *ACS Photonics*, 2019, 6: 538–544
- 12 Sun D, Li T, Yang B, et al. Research on polarization performance of InGaAs focal plane array integrated with superpixel-structured subwavelength grating. *Opt Express*, 2019, 27: 9447
- 13 Sun D, Feng B, Yang B, et al. Design and fabrication of an InGaAs focal plane array integrated with linear-array polarization grating. *Opt Lett*, 2020, 45: 1559–1562
- 14 Kim J O, Yoon S, Kang B, et al. Linear polarization detection of type II InAs/GaSb superlattice infrared photodetectors. In: *Proceedings of Asia Communications and Photonics Conference*, Hong Kong, 2015
- 15 Müller R, Gramich V, Wauro M, et al. High operating temperature InAs/GaSb type-II superlattice detectors on GaAs substrate for the long wavelength infrared. *Infrared Phys Tech*, 2019, 96: 141–144
- 16 Harchanko J, Pezzaniti L, Chenault D, et al. Comparing a MWIR and LWIR polarimetric imager for surface swimmer detection. In: *Proceedings of SPIE*, 2008
- 17 Gurton K P, Felton M. Remote detection of buried land-mines and IEDs using LWIR polarimetric imaging. *Opt Express*, 2012, 20: 22344–22359
- 18 Felton M, Gurton K P, Pezzaniti J L, et al. Measured comparison of the crossover periods for mid- and long-wave IR (MWIR and LWIR) polarimetric and conventional thermal imagery. *Opt Express*, 2010, 18: 15704–15713
- 19 Pezzaniti J L, Chenault D, Gurton K, et al. Detection of obscured targets with IR polarimetric imaging. In: *Proceedings of SPIE*, 2014
- 20 Kristan P G, Alex J Y, Gorden V. LWIR polarimetry for enhanced facial recognition in thermal imagery. In: *Proceedings of SPIE*, 2014
- 21 Dai J, Boffety M, Goudail F. Effect of imaging geometry and noise model on polarimetric contrast optimization. *Appl Opt*, 2019, 58: 2100–2111
- 22 Wendt J R, Carter T R, Samora S, et al. Micropolarizing device for long wavelength infrared polarization imaging. 2006
- 23 Kristan G, Melvin F, Robert M, et al. MidIR and LWIR polarimetric sensor comparison study. In: *Proceedings of SPIE*, 2010
- 24 Pors A, Nielsen M G, Bozhevolnyi S I. Plasmonic metagratings for simultaneous determination of Stokes parameters. *Optica*, 2015, 2: 716–723
- 25 Yang Z Y, Wang Z K, Wang Y X, et al. Generalized Hartmann-Shack array of dielectric metalens sub-arrays for polarimetric beam profiling. *Nat Commun*, 2018, 9: 4607
- 26 Schott J R. Fundamentals of polarimetric remote sensing, In: *Proceedings of SPIE*, 2009
- 27 Wu Z, Powers P E, Sarangan A M, et al. Optical characterization of wiregrid micropolarizers designed for infrared imaging polarimetry. *Opt Lett*, 2008, 33: 1653–1655
- 28 Xia J, Yuan Z H, Wang C, et al. Design and fabrication of a linear polarizer in the 8–12  $\mu\text{m}$  infrared region with multilayer nanogratings. *OSA Continuum*, 2019, 2: 1683–1692